

Global stability of flow past a cylinder with centreline symmetry

BHASKAR KUMAR, JACOB JOHN KOTTARAM,
AMIT KUMAR SINGH AND SANJAY MITTAL†

Department of Aerospace Engineering, Indian Institute of Technology,
Kanpur, UP 208 016, India

(Received 23 July 2008 and in revised form 23 March 2009)

Global absolute and convective stability analysis of flow past a circular cylinder with symmetry conditions imposed along the centreline of the flow field is carried out. A stabilized finite element formulation is used to solve the eigenvalue problem resulting from the linearized perturbation equation. All the computations carried out are in two dimensions. It is found that, compared to the unrestricted flow, the symmetry conditions lead to a significant delay in the onset of absolute as well as convective instability. In addition, the onset of absolute instability is greatly affected by the location of the lateral boundaries and shows a non-monotonic variation. Unlike the unrestricted flow, which is associated with von Kármán vortex shedding, the flow with centreline symmetry becomes unstable via modes that are associated with low-frequency large-scale structures. These lead to expansion and contraction of the wake bubble and are similar in characteristics to the low-frequency oscillations reported earlier in the literature. A global linear convective stability analysis is utilized to find the most unstable modes for different speeds of the disturbance. Three kinds of convectively unstable modes are identified. The ones travelling at very low streamwise speed are associated with large-scale structures and relatively low frequency. Shear layer instability, with relatively smaller scale flow structures and higher frequency, is encountered for disturbances travelling at relatively larger speed. For low blockage a new type of instability is found. It travels at relatively high speed and resembles a swirling flow structure. As opposed to the absolute instability, the convective instability appears at much lower Re and its onset is affected very little by the location of the lateral boundaries. Analysis is also carried out for determining the convective stability of disturbances that travel in directions other than along the free stream. It is found that the most unstable disturbances are not necessarily the purely streamwise travelling ones. Disturbances that move purely in the cross-stream direction can also be convectively unstable. The results from the linear stability analysis are confirmed by carrying out direct time integration of the linearized disturbance equations. The disturbance field shows transient growth by several orders of magnitude confirming that such flows act as amplifiers. Direct time integration of the Navier–Stokes equation is carried out to track the time evolution of both the large-scale low-frequency oscillations and small-scale shear layer instabilities. The critical Re for the onset of convective instability is compared with earlier results from local analysis. Good agreement is found.

† Email address for correspondence: smittal@iitk.ac.in

1. Introduction

Flows past bluff bodies are endowed with various kind of instabilities. For symmetric bodies, linear stability analysis of wake flows reveals the presence of two types of modes: symmetric and antisymmetric. Flow past a circular cylinder becomes unsteady at $Re \sim 47$ via an instability of the wake (Jackson 1987; Zebib 1987; Williamson 1989; Norberg 1994; Chen, Pritchard & Tavener 1995; Ding & Kawahara 1999; Morzynski, Afanasiev & Thiele 1999; Norberg 2001; Kumar & Mittal 2006a, b). The Reynolds number Re is based on the diameter of the cylinder. The resulting flow becomes asymmetric with respect to the wake centreline. Due to the loss of symmetry the instability is also referred to as symmetry breaking instability (Tang & Aubry 1997). It can be shown, via global linear stability analysis, that the loss of symmetry and the subsequent appearance of von Kármán shedding is related to the contrasting symmetry properties of the base flow and the unstable eigenmodes. In terms of the vorticity field the base flow is antisymmetric and loses stability to a symmetric mode of disturbance. Due to its oscillatory nature the instability is also referred as a Hopf bifurcation (Marsden & McCracken 1976). The unsteadiness develops into a periodic flow which has a different kind of symmetry called the spatio-temporal symmetry – a translation in time by half a period and subsequent reflection about the wake centreline takes the flow back to the initial state (Blackburn *et al.* 2005). The Strouhal number St related to the non-dimensional frequency of the unsteadiness at the onset of instability is 0.12, approximately, and continues to increase with Re . At larger Re the appearance of small-scale vortices due to the instability of the separated shear layer is observed (Prasad & Williamson 1997).

While the primary wake instability occurs due to the instability of a symmetric mode, both symmetric and antisymmetric modes may become unstable at larger Re . This complicates the flow considerably. Better understanding of the various modes of instabilities is expected if one can design investigations which allow one to study these instabilities separately. In this respect, we note that the primary wake instability can be suppressed by imposing a symmetry condition at the centreline. For example, the centreline can be forced to remain a streamline. This condition does not alter the base flow and the antisymmetric modes but eliminates the symmetric modes. Thus, such an arrangement helps us to identify those phenomenon which owe their origin to the instability of the modes that are antisymmetric. In particular, shear/mixing layer instabilities can be studied in addition to other antisymmetric unstable modes that might exist. In the past, wake flows have been investigated in great detail. In comparison, wakes with centreline symmetry have received less attention. The present effort is an attempt to investigate the flow past a cylinder with centreline symmetry.

There are two approaches to the linear stability analysis: local analysis of the assumed parallel flow and global non-parallel flow theory. In the local analysis the flow field is assumed to be locally parallel at different stations in the streamwise direction. Then, the absolute/convective nature of instability of the flow is determined at each station. On the other hand, global non-parallel analysis attempts to determine the stability of the entire flow field at once. Thus one obtains various temporal modes, their growth rate and frequencies. A global non-parallel approach is employed to carry out the present investigations. Both absolute as well as convective instabilities are considered. The absolute instability modes eventually lead to self-sustained oscillations which, therefore, appear as being intrinsic to the flow. In contrast, a convectively unstable flow results in disturbances that travel downstream as they grow (Huerre & Monkewitz 1990).

In the past, most of the stability studies of the wake with centreline symmetry have been carried out via local analysis. Koch (1985) investigated family of symmetric and asymmetric basic wake flows modelled with analytical functions. In his study shear layer was investigated as a limiting case of asymmetrical wake flows. It was found that at least one bifurcation point exists corresponding to time-attenuated convective instabilities. Huerre & Monkewitz (1985) investigated tangent hyperbolic profiles for the case of inviscid flows and showed that the flow becomes absolutely unstable when the velocity ratio, defined as the ratio of the difference to the sum of the velocity of the upper and lower streams, becomes larger than 1.315. Convective instability is observed in the range 0.84–1.315. Hultgren & Aggarwal (1987) considered a Gaussian velocity profile normalized with the maximum velocity. Though the main focus of their study was modes corresponding to the Kármán-type shedding they also investigated the flow with symmetry conditions enforced at the centreline. In the later case, antisymmetric modes were found to become unstable. The onset of convective instability was found to occur at $Re = 53$. The Re is based on the wake half-width and the maximum velocity difference for the local profile. Castro (2005) carried out similar computations and studied the effect of the location of lateral boundaries on the critical parameters. A free-slip condition was imposed at the lateral boundaries. It was found that the critical Re for the convective as well as absolute instability increases when the lateral boundaries are brought closer.

In another interesting study, Fasel & Postl (2006) carried out direct numerical simulation of a laminar separation bubble formed on a flat plate by introducing a volume force field. The study was carried out for steady, marginally unsteady, unsteady and highly unsteady separation bubbles. In each case the convective/absolute nature of instability was determined for a typical flow profile. It was found that the steady flow profile was highly convectively unstable. The Fourier amplitude of the spanwise disturbance vorticity got magnified by several orders of magnitude in the streamwise direction. This indicated that extremely small background disturbances could lead to large-disturbance wave and vortices. The fluid system in this case acts as an amplifier – a characteristic of convectively unstable flows.

Experimental investigations in the past have reported the presence of shear layer vortices that arise due to the Kelvin–Helmholtz mechanism. Various values of the critical Reynolds number Re_c , at which this instability is first observed, have been reported in the literature. Bloor (1964) observed the shear layer instability for Re larger than 1300. Unal & Rockwell (1988) reported that they did not observe the shear layer transition waves for $Re < 1900$ using flow visualization technique. Prasad & Williamson (1997) found that the end conditions affected the Re_c ; it is ~ 1200 for parallel shedding conditions and significantly higher (~ 2600) for end conditions that result in oblique shedding. Recently, Rajagopalan & Antonia (2005), using a single hot wire probe, found that the Re for the onset of the shear layer instability is 740. An interesting case is that of Gerrard (1978). He observed the shear layer instability to occur as low as $Re = 350$. Through computations, Mittal (2008) investigated the receptivity of the separated shear layer for the $Re = 300$ flow past a cylinder to pulsatile inflow. It was found that the shear layer instability can be excited in a certain range of frequencies and at Re as low as 100. In a very recent study Mittal, Kottaram & Kumar (2008) showed that the origin of these kind of instabilities can be traced down to very low values of Re . However, at these low Re this convective instability has a very low growth rate compared to that of the regular Kármán shedding and, therefore, it cannot be observed in the experiments.

Another type of instability, relevant in the present context, is the low-frequency oscillations observed in the turbulent wake bubbles (Alam & Sandham 2000; Manhart & Fredrich 2001). The precise nature and the cause of these oscillations has been an issue of debate in the literature. Hudy *et al.* (2003) suggested that an inherent absolute instability near the middle of the recirculation region is the basic driver for the unsteadiness of the bubble. Generally, experiments and computations carried for two-dimensional bubble have been at high enough Re where the flow is naturally turbulent. Castro (2005), via time integration of the Navier–Stokes equations, showed the presence of these low-frequency oscillations at much lower Re , in the case of symmetrically separated wake produced by imposing centreline symmetry in flow past a normal flat plate.

In this paper we carry out global stability analysis of the flow past a cylinder with centreline symmetry to understand the absolute and convective instabilities associated with the flow. The global modes that lead to the low-frequency and large-scale expansion/contraction of the wake bubble and the small-scale structures due to the Kelvin–Helmholtz instability of the separated shear layer are identified. Extensive computations are carried out to determine the instability modes associated with different velocities. Particular attention is paid to those which move in the streamwise direction. The growth rate of the instabilities is sensitive to the amount of reverse flow. The region of the flow occupied by the recirculation bubble is related to, among other parameters, the blockage. The location of the lateral boundaries is, therefore, crucial in the stability of the flow. The growth rate of the instability modes is found to be greatly affected by the location of the lateral boundaries. The onset of instability for the stationary modes shows a non-monotonic variation. For the case of low blockage we find instability modes, perhaps not reported earlier, which give rise to spanwise swirling structures or horizontal tornadoes travelling at relatively high speeds.

In addition to the stability analysis, full nonlinear equations have also been integrated in time to study the time evolution of the flow field. It is found that both the low-frequency and shear layer modes are present in the flow. Thus an explanation for the appearance of various instabilities is offered in terms of the linear stability of the base flow.

A stabilized finite element formulation is used for the study. The streamline-upwind/Petrov–Galerkin (SUPG) and pressure-stabilizing/Petrov–Galerkin (PSPG) stabilization technique (Tezduyar *et al.* 1992) is employed to stabilize the computations against spurious numerical oscillations. Equal-order-interpolation bilinear functions for velocity and pressure are employed. For unsteady computations, we utilize a second-order-in-time procedure to carry out the time integration of the flow equations. The algebraic equation systems resulting from the finite element discretization of the flow equations are solved using the generalized minimal residual (GMRES) technique (Saad & Schultz 1986) in conjunction with diagonal preconditioners. The formulation for the linear stability analysis with the stabilized finite element method, being used here, was proposed in one of our earlier articles (Mittal & Kumar 2003). First, the steady-state solutions at various Re are obtained by solving the governing equations by dropping the unsteady terms and progressively increasing the Re . The linear stability analysis of these steady states involves the solution to an eigenvalue problem. A subspace iteration procedure (Morzynski *et al.* 1999) in conjunction with shift-invert transformation is utilized. Double precision arithmetic is used in all the computations. The paper is arranged in the following sequence. In the §2, we present the governing equations. The stabilized finite element formulation to carry out the direct time integration of the governing equations and for the linear stability

analysis are presented in §3. This is followed by problem set-up and boundary conditions presented in §4. The results are presented and discussed in §5. We end with conclusions in §6.

2. The governing equations

2.1. The incompressible flow equations

Let $\Omega \subset \mathbb{R}^{n_{sd}}$ and $(0, T)$ be the spatial and temporal domains respectively, where n_{sd} is the number of space dimensions, and let Γ denote the boundary of Ω . The spatial and temporal coordinates are denoted by x and t . The Navier–Stokes equations governing incompressible fluid flow are

$$\rho \left(\frac{\partial \mathbf{u}}{\partial t} + \mathbf{u} \cdot \nabla \mathbf{u} \right) - \nabla \cdot \boldsymbol{\sigma} = \mathbf{0} \quad \text{on } \Omega \times (0, T), \quad (1)$$

$$\nabla \cdot \mathbf{u} = 0 \quad \text{on } \Omega \times (0, T). \quad (2)$$

Here ρ , \mathbf{u} and $\boldsymbol{\sigma}$ are the density, velocity and the stress tensor, respectively. The stress tensor is written as the sum of its isotropic and deviatoric parts:

$$\boldsymbol{\sigma} = -p\mathbf{I} + \mathbf{T}, \quad \mathbf{T} = 2\mu\boldsymbol{\varepsilon}(\mathbf{u}), \quad \boldsymbol{\varepsilon}(\mathbf{u}) = \frac{1}{2}((\nabla \mathbf{u}) + (\nabla \mathbf{u})^T), \quad (3)$$

where p and μ are the pressure and coefficient of dynamic viscosity, respectively. The above set of equations can be solved along with suitable initial and boundary conditions to obtain the time evolution of the flow field. The steady-state solution can be computed by simply dropping the time derivative term from (1).

2.2. Equations for the perturbation

We decompose the unsteady solution as a combination of the steady-state solution and perturbation:

$$\mathbf{u} = U + \mathbf{u}', \quad p = P + p'. \quad (4)$$

Here, U and P represent the steady-state solution while \mathbf{u}' and p' are the perturbation fields of the velocity and pressure, respectively. Substituting (4) in (1)–(2) and subtracting from them the equations for steady flow one obtains

$$\rho \left(\frac{\partial \mathbf{u}'}{\partial t} + \mathbf{u}' \cdot \nabla U + U \cdot \nabla \mathbf{u}' + \mathbf{u}' \cdot \nabla \mathbf{u}' \right) - \nabla \cdot \boldsymbol{\sigma}' = \mathbf{0} \quad \text{on } \Omega \times (0, T), \quad (5)$$

$$\nabla \cdot \mathbf{u}' = 0 \quad \text{on } \Omega \times (0, T). \quad (6)$$

Here, $\boldsymbol{\sigma}'$ is the stress tensor for the perturbed solution computed using (3).

2.3. Linearized equations for the perturbation

Assuming that the perturbation field is small, the nonlinear term from (5) is dropped to obtain the linearized momentum equation for the perturbation. The continuity equation remains as it is. The linearized disturbance equations are

$$\rho \left(\frac{\partial \mathbf{u}'}{\partial t} + \mathbf{u}' \cdot \nabla U + U \cdot \nabla \mathbf{u}' \right) - \nabla \cdot \boldsymbol{\sigma}' = \mathbf{0} \quad \text{on } \Omega \times (0, T), \quad (7)$$

$$\nabla \cdot \mathbf{u}' = 0 \quad \text{on } \Omega \times (0, T). \quad (8)$$

2.4. Equations for the linear stability analysis

Following the idea proposed by Mittal & Kumar (2007) we note that the global linear stability analysis of a non-parallel flow can be carried out in a frame moving with uniform velocity with respect to the laboratory frame. Let \mathbf{x} denote the position vector of a point in the flow field with respect to the laboratory frame. Let \mathbf{z} be its position vector in another frame that is moving with velocity \mathbf{c} with respect to the laboratory frame. The transformations which relate the two frames are

$$\mathbf{x} = \mathbf{z} + \mathbf{c}t, \quad \nabla_{\mathbf{x}} = \nabla_{\mathbf{z}}, \quad \frac{\partial}{\partial t} \Big|_{\mathbf{x}} = \frac{\partial}{\partial t} \Big|_{\mathbf{z}} - \mathbf{c} \cdot \nabla_{\mathbf{z}}. \quad (9)$$

We further assume that the disturbances are of the following form:

$$\mathbf{u}'(\mathbf{x}, t) = \hat{\mathbf{u}}(\mathbf{x} - \mathbf{c}t) e^{\lambda t}, \quad (10)$$

$$p'(\mathbf{x}, t) = \hat{p}(\mathbf{x} - \mathbf{c}t) e^{\lambda t}. \quad (11)$$

Such a perturbation would be seen as moving with velocity \mathbf{c} in the laboratory frame while it will appear stationary in the moving frame. Substituting (10)–(11) in (7)–(8) we get

$$\rho(\lambda \hat{\mathbf{u}} + \hat{\mathbf{u}} \cdot \nabla_{\mathbf{z}} U + (U - \mathbf{c}) \cdot \nabla_{\mathbf{z}} \hat{\mathbf{u}}) - \nabla_{\mathbf{z}} \cdot \hat{\boldsymbol{\sigma}} = \mathbf{0} \quad \text{on } \Omega \quad (12)$$

$$\nabla_{\mathbf{z}} \cdot \hat{\mathbf{u}} = 0 \quad \text{on } \Omega. \quad (13)$$

It is important to note that the base flow $U(\mathbf{x})$ is computed in the laboratory frame. However, in (12)–(13), it is to be interpreted as $U(\mathbf{z} + \mathbf{c}t)$. Therefore, in the moving frame, the base flow varies with time. At $t = 0$, $\mathbf{z} = \mathbf{x}$ and one can use the same base flow as computed in the stationary frame. At other time instants \mathbf{z} and \mathbf{x} are different and the perturbation encounters different base flow at different times. Therefore, this analysis, for determining the global convective instability, is valid in an instantaneous sense. $\lambda(\mathbf{c})$ is the eigenvalue of the fluid system and governs its stability. In general, $\lambda(\mathbf{c}) = \lambda_r(\mathbf{c}) + i\lambda_i(\mathbf{c})$ where, $\lambda_r(\mathbf{c})$ and $\lambda_i(\mathbf{c})$ are the real and imaginary parts, respectively. Growth of a perturbation, indicated by $\lambda_r(\mathbf{c}) > 0$, would be seen as a global absolute instability in the moving frame, while in the laboratory frame it will appear as globally convectively unstable. It follows that the flow is globally convectively unstable if there exists a \mathbf{c} for which $\lambda_r(\mathbf{c}) > 0$, provided $\lambda_r(\mathbf{0}) < 0$. When $\lambda_r(\mathbf{0}) > 0$, the flow is globally absolutely unstable. The boundary conditions for $(\hat{\mathbf{u}}, \hat{p})$ are the homogeneous versions of the ones for (U, P) .

3. The finite element formulation

Consider a finite element discretization of Ω into subdomains Ω^e , $e = 1, 2, \dots, n_{el}$, where n_{el} is the number of elements. Based on this discretization, for velocity and pressure perturbation fields we define the finite element trial function spaces $\hat{\mathcal{S}}_u^h$ and $\hat{\mathcal{S}}_p^h$, and weighting function spaces $\hat{\mathcal{V}}_u^h$ and $\hat{\mathcal{V}}_p^h$. Here, the superscript ' h ' represents spatial discretization. These function spaces are selected by taking the Dirichlet boundary conditions into account, as subsets of $[\mathbf{H}^{1h}(\Omega)]^2$ and $\mathbf{H}^{1h}(\Omega)$, where $\mathbf{H}^{1h}(\Omega)$ is the finite-dimensional function space over Ω .

3.1. The incompressible flow equations

The stabilized finite element formulation of (1) and (2) is written as follows: find $\mathbf{u}^h \in \mathcal{S}_u^h$ and $p^h \in \mathcal{S}_p^h$ such that $\forall \mathbf{w}^h \in \mathcal{V}_u^h$ and $q^h \in \mathcal{V}_p^h$

$$\begin{aligned} & \int_{\Omega} \mathbf{w}^h \cdot \rho \left(\frac{\partial \mathbf{u}^h}{\partial t} + \mathbf{u}^h \cdot \nabla \mathbf{u}^h \right) d\Omega + \int_{\Omega} \boldsymbol{\varepsilon}(\mathbf{w}^h) : \boldsymbol{\sigma}(p^h, \mathbf{u}^h) d\Omega \\ & + \int_{\Omega} q^h \nabla \cdot \mathbf{u}^h d\Omega + \sum_{e=1}^{n_{el}} \int_{\Omega^e} \frac{1}{\rho} (\tau_{SUPG} \rho \mathbf{u}^h \cdot \nabla \mathbf{w}^h + \tau_{PSPG} \nabla q^h) . \\ & \left[\rho \left(\frac{\partial \mathbf{u}^h}{\partial t} + \mathbf{u}^h \cdot \nabla \mathbf{u}^h \right) - \nabla \cdot \boldsymbol{\sigma}(p^h, \mathbf{u}^h) \right] d\Omega^e \\ & + \sum_{e=1}^{n_{el}} \int_{\Omega^e} \tau_{LSIC} \nabla \cdot \mathbf{w}^h \rho \nabla \cdot \mathbf{u}^h d\Omega^e = \int_{\Gamma_h} \mathbf{w}^h \cdot \mathbf{h}^h d\Gamma. \end{aligned} \quad (14)$$

In the variational formulation given by (14), the first three terms on the left-hand side and the one on the right-hand side constitute the Galerkin formulation of the problem. To give stability to the basic formulation, a series of element-level integrals are added. The first series of element-level integrals are the SUPG and PSPG stabilization terms added to the variational formulations (Tezduyar *et al.* 1992). The SUPG formulation for convection dominated flows was introduced by Hughes & Brooks (1979) and Brooks & Hughes (1982). The Petrov–Galerkin term for Stokes flows, to admit the use of equal-order interpolations for velocity and pressure without producing oscillations in the pressure field, was proposed by Hughes, Franca & Balestra (1986). Tezduyar *et al.* (1992) proposed a formulation using the SUPG and PSPG stabilizations for finite-Reynolds-number flows. The second series of element level integrals are stabilization terms based on the least squares of the divergence-free condition on the velocity field. The definition of the stabilization parameters being used is the same as presented in an earlier article (Kumar & Mittal 2006a).

3.2. The perturbation equation

The application of the stabilized finite element method to the perturbation equations, (5) and (6), results in the following formulation: find $\hat{\mathbf{u}}^h \in \hat{\mathcal{S}}_u^h$ and $\hat{p}^h \in \hat{\mathcal{S}}_p^h$ such that $\forall \hat{\mathbf{w}}^h \in \hat{\mathcal{V}}_u^h$ and $\hat{q}^h \in \hat{\mathcal{V}}_p^h$

$$\begin{aligned} & \int_{\Omega} \mathbf{w}^h \cdot \rho \left(\frac{\partial \mathbf{u}'^h}{\partial t} + U^h \cdot \nabla \mathbf{u}'^h + \mathbf{u}'^h \cdot \nabla U^h + \mathbf{u}'^h \cdot \nabla \mathbf{u}'^h \right) d\Omega + \int_{\Omega} \boldsymbol{\varepsilon}(\mathbf{w}^h) : \boldsymbol{\sigma}(\mathbf{p}'^h, \mathbf{u}'^h) d\Omega \\ & + \int_{\Omega} \mathbf{q}^h \nabla \cdot \mathbf{u}'^h d\Omega + \sum_{e=1}^{n_{el}} \int_{\Omega^e} \frac{1}{\rho} (\tau_{SUPG} \rho U^h \cdot \nabla \mathbf{w}^h + \tau_{PSPG} \nabla \mathbf{q}^h) . \\ & \left[\rho \left(\frac{\partial \mathbf{u}'^h}{\partial t} + U^h \cdot \nabla \mathbf{u}'^h + \mathbf{u}'^h \cdot \nabla U^h + \mathbf{u}'^h \cdot \nabla \mathbf{u}'^h \right) - \nabla \cdot \boldsymbol{\sigma}(\mathbf{p}'^h, \mathbf{u}'^h) \right] d\Omega^e \\ & + \sum_{e=1}^{n_{el}} \int_{\Omega^e} \tau_{LSIC} \nabla \cdot \mathbf{w}^h \rho \nabla \cdot \mathbf{u}'^h d\Omega^e = 0. \end{aligned} \quad (15)$$

The variational formulation given by (15) includes the nonlinear term arising from the convection of the disturbance. The formulation for the linearized disturbance

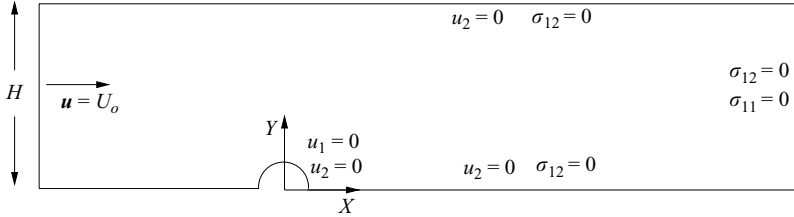


FIGURE 1. Flow past a half-cylinder: schematic of the computational domain and boundary conditions.

equations given by (7) and (8) can be obtained from (15) by simply dropping the terms quadratic in \mathbf{u}^h .

3.3. The linear stability equations

Let $\hat{\mathcal{S}}_u^h$ and $\hat{\mathcal{S}}_p^h$ be the finite element trial function spaces and $\hat{\mathcal{V}}_u^h$ and $\hat{\mathcal{V}}_p^h$ the weighting function spaces for the perturbations in the velocity and pressure fields, respectively. The finite element formulation for the perturbation equations, (12) and (13), is given as: find $\hat{\mathbf{u}}^h \in \hat{\mathcal{S}}_u^h$ and $\hat{p}^h \in \hat{\mathcal{S}}_p^h$ such that $\forall \hat{\mathbf{w}}^h \in \hat{\mathcal{V}}_u^h$ and $\hat{q}^h \in \hat{\mathcal{V}}_p^h$

$$\begin{aligned} & \int_{\Omega} \hat{\mathbf{w}}^h \cdot \rho (\lambda \hat{\mathbf{u}}^h + (U^h - c) \cdot \nabla \hat{\mathbf{u}}^h + \hat{\mathbf{u}}^h \cdot \nabla U^h) d\Omega + \int_{\Omega} \boldsymbol{\epsilon}(\hat{\mathbf{w}}^h) : \boldsymbol{\sigma}(\hat{p}^h, \hat{\mathbf{u}}^h) d\Omega \\ & + \int_{\Omega} \hat{q}^h \nabla \cdot \hat{\mathbf{u}}^h d\Omega + \sum_{e=1}^{n_{el}} \int_{\Omega_e} \frac{1}{\rho} (\tau_{SUPG} \rho (U^h - c) \cdot \nabla \hat{\mathbf{w}}^h + \tau_{PSPG} \nabla \hat{q}^h) . \\ & [\rho (\lambda \hat{\mathbf{u}}^h + (U^h - c) \cdot \nabla \hat{\mathbf{u}}^h + \hat{\mathbf{u}}^h \cdot \nabla U^h) - \nabla \cdot \boldsymbol{\sigma}(\hat{p}^h, \hat{\mathbf{u}}^h)] d\Omega^e \\ & + \sum_{e=1}^{n_{el}} \int_{\Omega^e} \tau_{LSIC} \nabla \cdot \hat{\mathbf{w}}^h \rho \nabla \cdot \hat{\mathbf{u}}^h d\Omega^e = 0. \end{aligned} \quad (16)$$

The stabilization coefficients for this formulation are based on the steady-state velocity field U^h .

3.4. The eigenvalue problem

Equation (16) leads to a generalized eigenvalue problem of the form $\mathbf{A}\mathbf{X} - \lambda \mathbf{B}\mathbf{X} = 0$, where \mathbf{A} and \mathbf{B} are non-symmetric matrices. The subspace iteration method (Stewart 1975) in conjunction with shift-invert transformation is used to solve the eigenvalue problem.

4. Problem set-up

4.1. Computational domain and boundary conditions

A schematic of the computational domain and the boundary conditions used in the present work is shown in the figure 1. To capture the modes that are symmetric with respect to the wake centreline only one-half of the cylinder is considered. The lateral boundary is located at a distance H from the centre of the cylinder. Computations are carried out for various values of H . The upstream and downstream boundaries are located at $50D$ and $150D$, respectively, from the centre of the cylinder. A free-stream value U_o is assigned to the velocity at the upstream boundary. At the downstream boundary, a Neumann-type boundary condition for the velocity is specified that corresponds to zero stress vector. On the upper and lower boundaries a 'slip-wall'

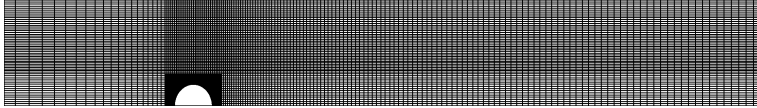


FIGURE 2. Flow past a half-cylinder: close-up view of a typical finite element mesh.

boundary condition is employed, i.e. the component of velocity normal to and the component of stress vector along these boundaries are prescribed a zero value. For the linear stability analysis, the boundary conditions are the homogeneous versions of the ones used for determining the steady-state solutions. A typical finite element mesh is shown in the figure 2. Four noded quadrilateral elements with equal order interpolation for velocity and pressure are employed. Sufficient grid points are used close to the cylinder to resolve the boundary layer and separating shear layer.

4.2. The non-dimensional parameters

The radius of the cylinder R is used for non-dimensionalizing the length scales while the free stream speed U is used as the characteristic speed. Time is non-dimensionalized with R/U . The Reynolds number Re is defined as UD/ν , ν being the kinematic viscosity of the fluid and D , the diameter. The cross-stream width of the domain H is expressed in terms of R . For the linear stability analysis, each component of the frame velocity c is non-dimensionalized with U . Another parameter that is referred to is the Strouhal number, St . It is defined as fD/U , where f is the frequency of signal of interest. The drag and lift coefficients per unit length are represented by C_D and C_L , respectively. They are computed by performing an integration, that involves the pressure and viscous stresses, around the circumference of the cylinder and non-dimensionalized with respect to the dynamic pressure and diameter of the cylinder.

5. Results

5.1. Steady flow

The time-dependent terms in (1) and (2) are dropped to compute the steady flow past a half-cylinder. We note that the steady flow past a circular cylinder is symmetric about the wake centreline. Hence the flow being computed here also represents the steady flow past a full cylinder. Computations are carried for various values of H and the results compared with those presented by earlier researchers. The steady flow characteristics like the length and width of the wake bubble, maximum vorticity on the surface of the cylinder and drag coefficient have been extensively studied in the past. It is found, both from the theoretical results as well as from computations (Smith 1979; Fornberg 1985; Fornberg 1991; Gajjar & Azzam 2004), that the bubble length increases linearly with Re . Smith (1979) suggested that the width of the wake bubble grows as $O(Re^{1/2})$. Fornberg (1985) showed that it grows as $O(Re^{1/2})$ up to $Re = 300$ and increases linearly thereafter. The asymptotic nature of the eddy structure in the case of bluff body flows was revealed by Chernyshenko (1988). Both the length and the width of the wake bubble were reported to scale as $O(Re)$. Later numerical computations by Fornberg (1991) conformed with these estimates. Gajjar & Azzam showed that although the width grows initially, for high enough Re it is limited by the blockage and hence gets saturated. Recently, Griffith *et al.* (2007) carried out an investigation of a partially blocked two-dimensional channel across a range of Re

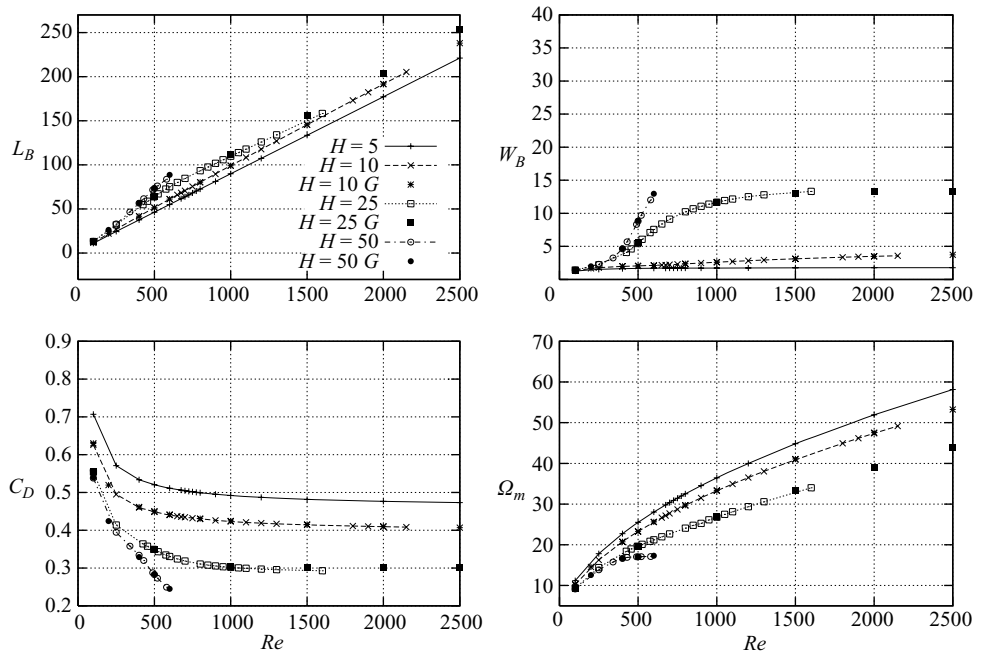


FIGURE 3. Steady flow past a circular cylinder: variation of the bubble characteristics with Re . The results obtained from the present study are compared with those from Gajjar & Azzam (2004). The abbreviations used are: L_B , bubble length; W_B , bubble width; C_D , drag coefficient; Ω_m , maximum vorticity on the cylinder surface. In the figure, H refers to the domain half-width and G refers to results from Gajjar & Azzam (2004).

and blockage. Over the Re range considered the variation of the length of the first recirculation bubble is found to be approximately linear.

The present results are in very good agreement with those reported by Gajjar & Azzam (2004). All the results have been checked for grid independence. For example, the bubble length computed for $H = 10$ case, at $Re = 1000$, with two different finite element meshes consisting of 57 313 and 86 419 nodes, respectively, differ from each other by less than 0.1 %. As reported by Gajjar & Azzam the computations for $H = 50$ and beyond are very demanding on computational resources. With our computational resources we are unable to compute flows for $Re > 500$ accurately for $H = 50$. Figure 3 shows the variation of bubble characteristics with Re for various domain width. Good agreement with data from Gajjar & Azzam is apparent from this figure. The linear growth of bubble length with Re can be clearly observed.

With respect to the blockage the flow can be broadly classified in three categories. Following the nomenclature proposed by Gajjar & Azzam (2004), we refer to these as ‘Type I-III’ solutions. When the adjacent boundaries are extremely close to the cylinder the recirculation bubble is slender. The length of the bubble increases with increase in Re . $H = 5$ flow is typical of very high blockage. We refer to these as ‘Type I’ solutions. As the lateral walls are shifted away from the cylinder the solution changes to ‘Type II’. The flow begins to develop features, associated with low blockage close to the reattachment point. An unusual increase in the bubble width near the downstream end of the bubble is observed. This feature of the bubble is similar to that observed in the Sadovskii type of vortex (Sadovskii 1971) and was also observed by Gajjar & Azzam. The bubble length increases linearly with Re . However, the bubble width saturates for large Re . Flow for $H = 10$ shows this behaviour. Type III

solution is observed for even lower blockage cases, for example, with $H = 50$. Both the length as well as the width of the bubble become very large. A large Sadovskii vortex (Sadovskii 1971) is observed in the wake of the cylinder. While the length of the bubble increases linearly with Re , the bubble width is constrained by the lateral wall and, therefore, is expected to level out for large Re . Similar behaviour of the recirculation bubble was reported by Castro (2002) for steady flow past a cascade of flat plates in stratified fluid.

5.2. Linear stability analysis: global absolute instability

5.2.1. Variation with blockage

Having validated the steady flow results of the present study with those from earlier researchers we investigate their global stability characteristics. A stabilized finite element formulation of the linearized disturbance equations, given by (16), is utilized. First, the absolute stability of the flow is studied by carrying out the analysis for stationary disturbances, i.e. $c = 0$. In the rest of the article the phrase ‘absolute/convective’ should be understood in a global non-parallel sense and should not be confused with the usual meaning that they have in the local theory (Huerre & Monkewitz 1990), unless stated otherwise. We track the variation of the rightmost eigenvalue (most positive/least negative) with Re for various H .

Figure 4 shows the variation of the growth rate λ_r and Strouhal number St with Re for various values of H . Of interest, for each H , is the critical Re for which the flow becomes unstable. The effect of blockage is classified into three categories to highlight the variation of λ_r with Re . The top row of figure 4 shows the results for high blockage ($H \leq 15$). For this case, λ_r first increases with Re and then, after achieving a maximum value, reduces with further increase in Re . The second and third rows of figure 4 show the results for moderate ($16 \leq H \leq 20$) and low blockage ($H \geq 25$), respectively. For moderate blockage, a steep rise in λ_r with increase in Re is observed for $Re < 600$, approximately. This is followed by a mild increase in the growth rate with any further increase in Re . For low blockage our computations are restricted to $Re \sim 500$. The flow is found to be stable up to this Re . The critical Re for which the λ_r becomes positive is expected to be much higher. In fact, it is possible that the flow may not become absolutely unstable at all as it approaches the limit of unbounded flow. For all values of H the St , related to the imaginary part of the eigenvalue with largest λ_r , decreases with increase in Re . In fact, for $H = 30$ and 50 the least stable mode for large Re is a real mode and, therefore, its St is zero.

Castro (2005), using arguments regarding the diffusion of vorticity from within an eddy of length L_B to outside the bubble, proposed that the time period of the instability should scale with ReH^2 . From the direct numerical simulations he found that on a log–log plot the variation of the time period of the instability is linear with ReH^2 . However, the slope is closer to 2 than to 1. Figure 5 shows the variation of the time period T of oscillation of the rightmost mode with ReH^2 on a log–log plot. Piecewise linear variation is seen for $H \leq 25$. The slope of the variation is different for various H and it also changes with Re , for each H . In general, the slope increases with increase in H . For $H = 5$ the slope of the graph is ~ 0.88 for lower Re and goes up to ~ 1.2 for large Re . For $H = 20$ the slope is ~ 4.22 for low Re and reduces to ~ 1.35 for large Re . The slope for $H = 50$ is 5, approximately, for low Re . It increases very rapidly with increase in Re . In fact, the St for the most unstable mode approaches 0, for large Re , as seen from figure 4. This seems to suggest that the time period becomes infinite as H increases and that the global mode might completely disappear for an unbounded flow. To confirm this, one would have to carry out computations

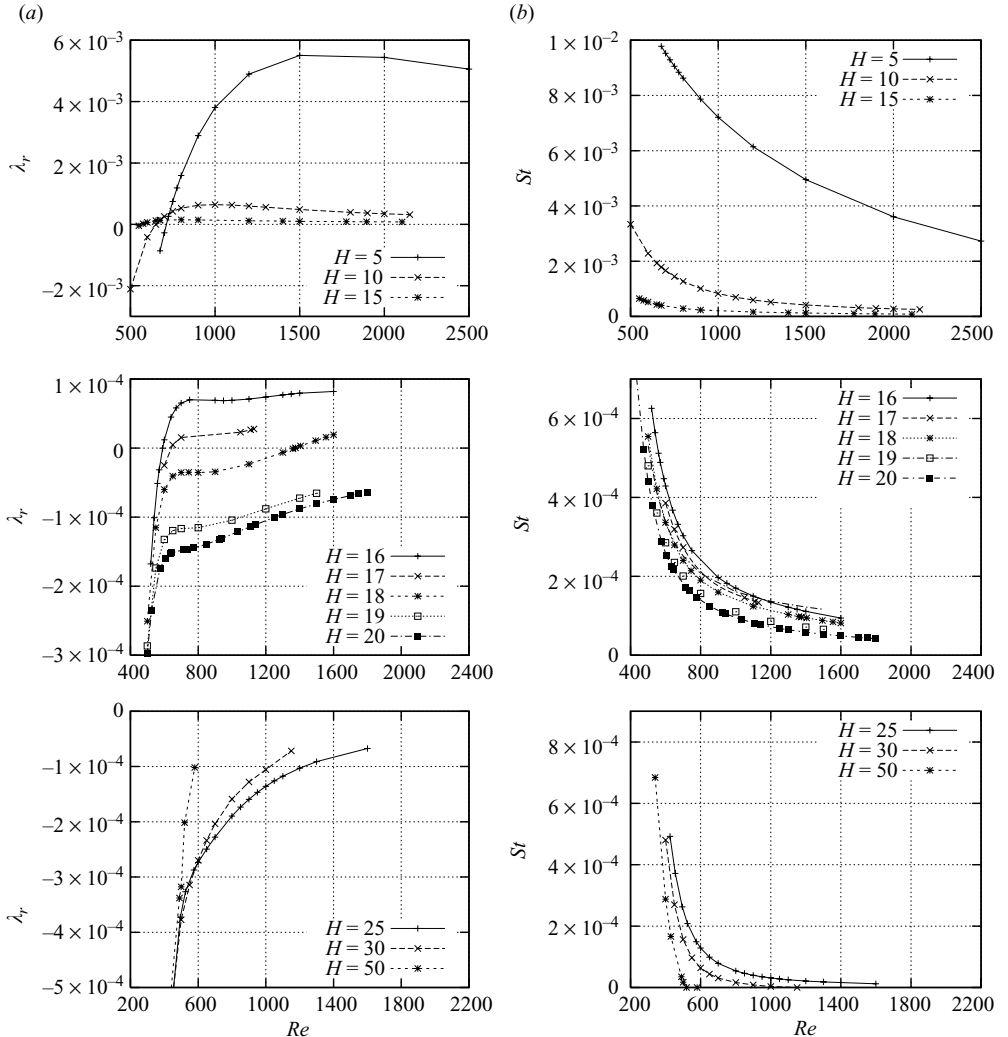


FIGURE 4. Linear stability analysis for flow past a half-cylinder for various H : variation of the growth rate of the most unstable mode (a) and St (b) with Re .

for larger H and Re . Unfortunately, this requires more computational resources than what we have access to at present.

Figure 6 shows the variation of the critical Reynolds number Re_c and the corresponding Strouhal number St_c with H . A non-monotonic variation of Re_c with H is observed. Re_c decreases as the wall is moved away from the cylinder for $H < 15$. For $H > 15$, the flow becomes more stable as the wall moves away further. Similar non-monotonic behaviour has been reported earlier for the onset of primary wake instability in the flow past a circular cylinder (see Kumar & Mittal 2006a, b). The presence of lateral boundaries has two competing effects on the disturbance field. When the lateral walls are close to the cylinder, they suppress the growth of the disturbances in the cross-stream direction owing to the $v = 0$ condition prescribed on the walls. However, they are also responsible for the local acceleration of the flow, thereby, subjecting the cylinder to an apparent higher Re flow and, therefore, making

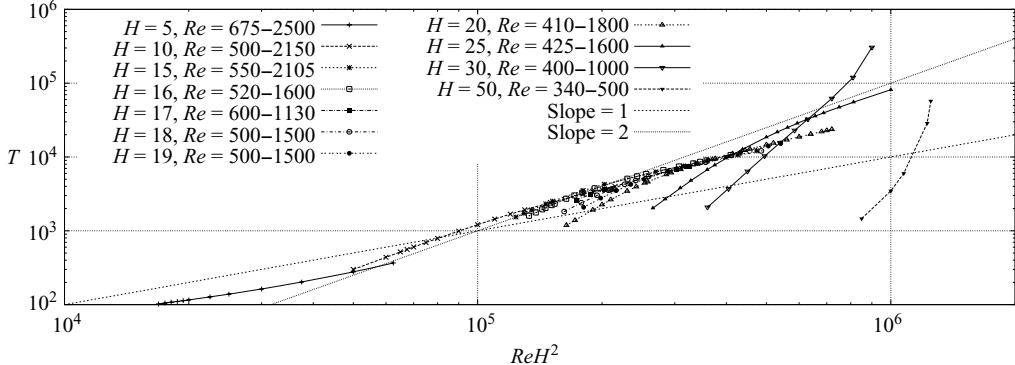


FIGURE 5. Linear stability analysis for flow past a half-cylinder for various H and Re : variation of the time period with ReH^2 of the most unstable mode. The lines with slopes 1 and 2 are also shown.

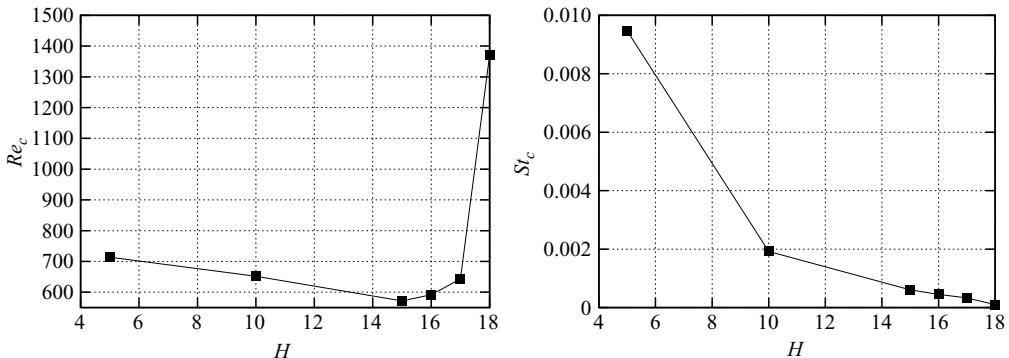


FIGURE 6. Linear stability analysis for flow past a half-cylinder: variation of the critical Reynolds number Re_c for absolute instability and the associated Strouhal number St_c with H .

it more unstable. These two effects oppose each other and result in a non-monotonic variation of Re_c with H . For very low H the former effect dominates; the stabilizing effect of the walls reduce as they are moved away. Therefore, Re_c decreases with increase in H . However, when the walls are taken sufficiently far away the stabilizing effect almost disappears. In this situation the decrease in blockage leads to an increase in Re_c . From figure 6 it is observed that St_c monotonically decreases with increase in H .

5.2.2. Eigenmodes at the onset of instability

Figure 7 shows the vorticity field of the real part of the most unstable eigenmode for various blockage. The stagnation streamline for the steady state is also shown. The Re for each value of H , for which the eigenmode is shown, is a little beyond the onset of instability. In all cases a bubble-like disturbance is observed in the wake of the cylinder which increases in size with increase in H . It occupies the entire recirculation zone of the steady flow. For future reference, we refer to this mode as the ‘bubble mode’. For higher blockage, as is the case with the recirculation bubble of the base flow, the bubble-like structure of the disturbance field is slender; its width is constrained by the lateral walls. In all the figures in this article with grey-scale shading the background shade of grey corresponds to a zero value. The lighter shades represent positive while

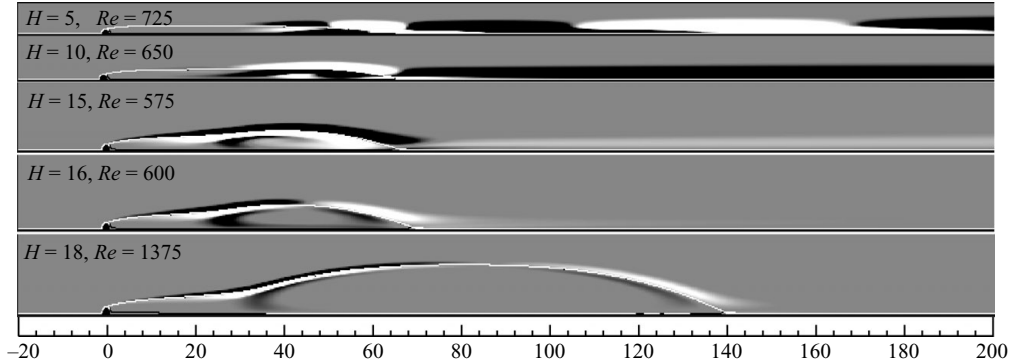


FIGURE 7. Flow past a half-cylinder: vorticity field of the real part of the rightmost eigenmodes for different lateral width of the domain; the modes shown were obtained for Re a little beyond the onset of instability. The stagnation streamline for the steady state is also shown in white colour.

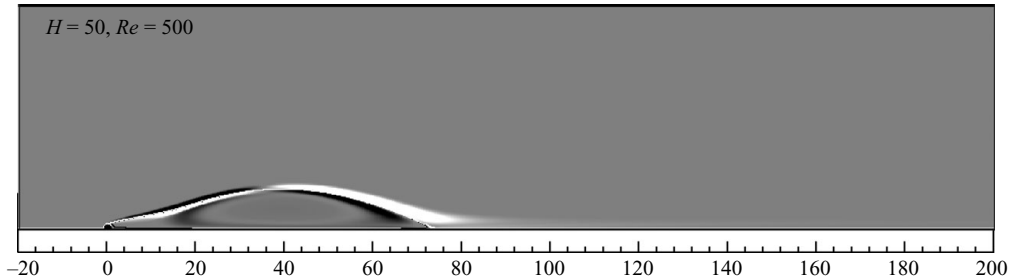


FIGURE 8. $Re = 500$, $H = 50$ flow past a half-cylinder: vorticity field of the real part of the least stable eigenmode. The stagnation streamline for the steady state is also shown in white colour.

the darker shades represent negative values. The length scale of the bubble/eddy structure at critical Re increases with increase in H . This corresponds to a decrease of St_c with increase in H as is also seen from figure 6. Figure 8 shows the real part of the vorticity field of the bubble mode at $Re = 500$ for low blockage ($H = 50$). Although it corresponds to the rightmost eigenvalue it is found to be stable.

Compared to the mode that causes von Kármán vortex shedding the bubble mode is associated with very low frequency. For example, for $H = 10$ the St_c is ~ 0.002 for the bubble mode while it is ~ 0.116 for the von Kármán vortex shedding mode for the full cylinder in an unbounded flow. To understand the nature of the instability we construct an unsteady flow by combining the steady flow and the complex conjugate pair of the eigenmode corresponding to the bubble mode. We choose $H = 10$ and $Re = 750$. Recall that the onset of instability for $H = 10$ occurs at $Re \sim 651.64$. It is found that it is this mode which leads to the low-frequency oscillations related to the streamwise expansion and contraction of a laminar separation bubble.

5.2.3. $H = 5$: the bubble mode at various Re

Figure 4 shows that the growth rate of the bubble mode, for high blockage, exhibits non-monotonic variation with Re . We offer a possible explanation for this observation. It is observed that as Re increases the mode recedes downstream. The time evolution of the kinetic energy of the disturbance field depends very significantly

on the transfer of kinetic energy from the base flow to the disturbance. It can be shown that the transfer term depends on the shear in the base flow. The shear in the base flow increases with Re . For each Re , it reduces as one moves downstream of the cylinder. Therefore, with increase in Re there is an increase in the transfer of energy from the base flow to the disturbance modes. However, beyond a certain Re , due to the downstream movement of the modes, the energy transfer from the base flow to the instability mode reduces. This anomalous behaviour causes the non-monotonic variation.

5.3. $H = 10$, $Re = 750$: unsteady computations

Figures 4 and 6 show that the steady flow for $H = 10$ loses stability beyond $Re \sim 651$. The unsteady flow equations, which include the nonlinear terms, are integrated in time to compute the evolution of the flow for $Re = 750$. The computations begin from the steady flow at the same Re . Since the steady base flow is linearly unstable the round off errors of the order of machine precision grow with time and the flow becomes unsteady. The top two rows of figure 9 show the time variation of the aerodynamic coefficients. The last row shows the crossflow component of velocity at a point located at $(7.56R, 0.133R)$ with respect to the centre of the cylinder. From these time histories we note that there are low-frequency oscillations which are accompanied by oscillations of higher temporal frequency. Although the large-scale oscillations are not very periodic, the average period is 1500 time units, approximately. This corresponds to $St \sim 0.00133$. The St predicted by the linear stability analysis is 0.00144. Figure 10 shows the vorticity field of the unsteady flow at various time instants. The expansion and contraction of the attached wake bubble is clearly observed in these visuals. Also observed from this figure is the significant reduction in the length and increase of the width of the bubble. This is due to the nonlinear effects that are accounted for in the direct numerical simulations. This also explains the difference in St from the linear stability analysis and the direct numerical simulation. The mean length of the bubble for the first cycle, at the beginning of the direct numerical simulation when the disturbances are small, is quite comparable to that for the steady solution. Numerical simulations were also carried out for $Re = 660$ which is close to the critical Re for the onset of the global absolute instability. Compared to $Re = 750$, the nonlinear effects were found to set in at a later time. Barring the appearance of small-scale shear layer vortices the flow for $Re = 660$ is virtually the same up to 500 non-dimensional time units as that obtained by the superimposition of the most unstable eigenmode and the steady base flow.

The convection of the large-scale vortices seen in the fifth, sixth and seventh frames of figure 10 is similar to that observed by Castro (2005). He also observed the shear layer vortices. It was reported that for high blockage they appear before the appearance of low-frequency modes. An opposite trend was observed for low blockage. However, not much attention was paid in his investigation to study the instability of the shear layer. Later in the paper, we relate the shear layer vortices to the convective instability of the flow. The results for $H = 10$ are typical of those for other cases with high blockage. For the low blockage case ($H = 50$) we carried out computations for $Re = 500$. In conformity with the results from linear stability analysis the flow is found to be stable in this situation and all disturbances eventually decay. As seen from figure 6 there is the rapid increase in the Re_c as the lateral boundaries are moved away. This behaviour is in contrast to that found by Castro (2005) for the flow normal to a plate with free-slip condition on the symmetry plane. His direct numerical simulations show a monotonic decrease in the Re_c with increase

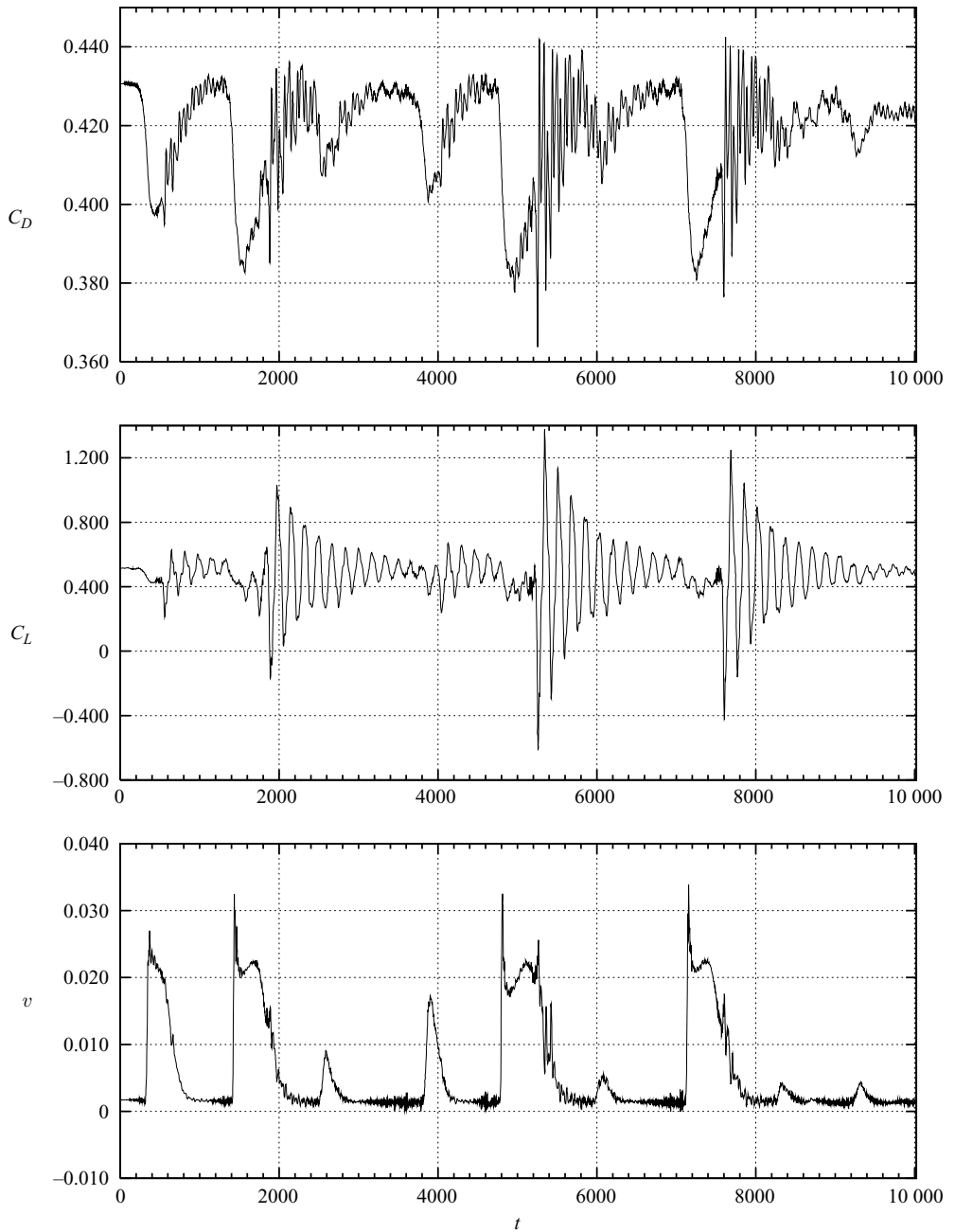


FIGURE 9. Direct time integration of the flow equations for the $H = 10$, $Re = 750$ flow past a half-cylinder: time histories of the force coefficients acting on the cylinder and the vertical component of velocity recorded at $x = 7.56R$ and $y = 0.133R$ from the centre of the cylinder.

in H (for $H \leq 30$). Two possibilities exist. Either the non-monotonicity reported in the present paper is specific to the cylinder or the flow past a normal flat plate may behave differently for lower blockage. More work is needed to resolve the apparent discrepancy. The agreement between the results from linear stability analysis and direct numerical simulations adds confidence to the present results.

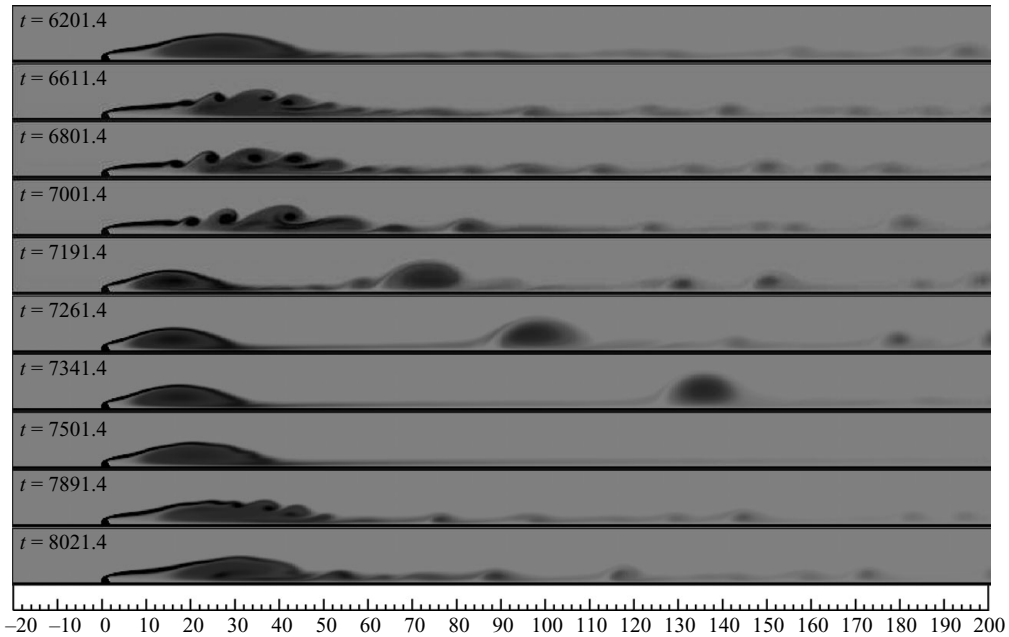


FIGURE 10. Direct time integration of the flow equations for the $H=10$, $Re=750$ flow past a half-cylinder: vorticity field of the flow computed at various time instants during, approximately, one cycle of the bubble mode.

5.4. Linear stability analysis: global convective instability

The results from the unsteady computations, shown in figures 9 and 10, indicate the presence of small-scale vortices in addition to the bubble mode. These vortices do not show a very well defined periodic behaviour and neither do they resemble any of the absolutely unstable modes determined from the linear stability analysis. This leads us to suspect that they might be a consequence of the convective instability of the base flow. To investigate this further we conduct global linear stability analysis of the flow to determine the convectively unstable modes. For each value of H and Re the analysis is carried out for various values of disturbance velocity $\mathbf{c}=(c_x, c_y)$.

5.4.1. $H = 10$, $Re = 500$ and $c_y = 0$

Figure 11 shows the growth rate and Strouhal number for the most unstable mode for various values of c_x . In these computations we track the disturbances which move in the streamwise direction, i.e. c_y is prescribed a zero value. To ensure the accuracy of results two finite element meshes are utilized: Mesh 1 with 57313 and Mesh 2 with 86419 grid points. The unsteady results from the direct numerical simulations, presented in the previous section, have been computed using Mesh 2. As seen from figure 11 the results from the two meshes are in excellent agreement. This confirms the adequacy of the spatial resolution being utilized here. The growth rate increases quite rapidly with c_x . At $c_x=0$ the growth rate is slightly negative. This reflects the marginal absolute stability of the flow. The flow is found to be unstable beyond $c_x \sim 0.05$. This marks the onset of convective instability of the flow. The St at the onset is 1.12×10^{-3} . Figure 12 shows the real part of the most unstable eigenmodes for various values of c_x . As c_x increases vortical structures reduce in size and shift upstream towards the cylinder. For $c_x=0.5$ and larger the eigenmodes exhibit very

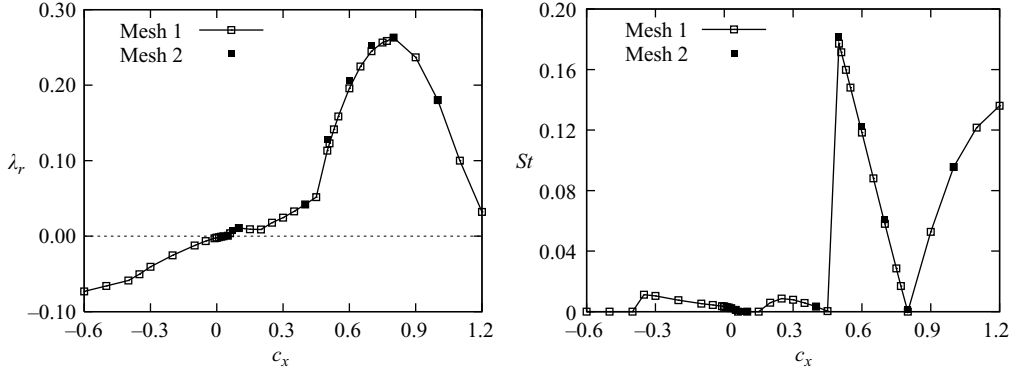


FIGURE 11. Linear stability analysis for the $H=10$, $Re=500$ flow past a half-cylinder: variation of growth rate and St with c_x ($c_y=0$) with two different finite element meshes. Mesh 1 consists of 57 313 nodes while Mesh 2 has 86 419 nodes.

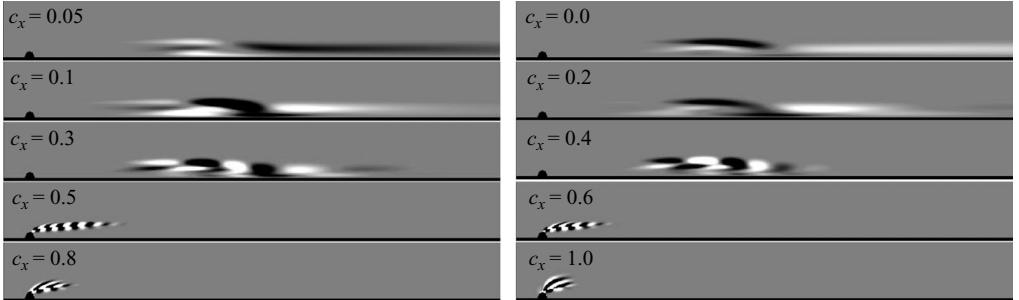


FIGURE 12. Linear stability analysis for the $H=10$, $Re=500$ flow past a half-cylinder: real part of the most unstable convective modes at various values of c_x . Only streamwise travelling modes are considered ($c_y=0$).

small-scale structures. Figure 11 shows that a sudden change in the St corresponding to the most unstable mode takes place at $c_x \sim 0.5$. This indicates a qualitative change in the type of mode which dominates the flow. The same can be seen from the variation of λ_r with c_x . This is because two different branches of the stability curve intersect at $c_x \sim 0.5$. The maximum growth rate is observed for $c_x \sim 0.8$. It is expected that if all the convectively unstable eigenmodes are introduced in the flow the one that moves with $c_x \sim 0.8$ will grow at the fastest rate and therefore dominate the flow. However, this being a convectively unstable mode, once the disturbance field is advected outside the domain the flow is expected to return to its undisturbed state.

5.4.2. Direct time integration of linearized disturbance equations

Direct time integration of the linearized disturbance equations is carried out to confirm the results from the linear stability analysis. The kinetic energy of the disturbance field in the flow domain Ω is defined as $E(t) = \frac{\rho}{2} \int_{\Omega} \mathbf{u}' \cdot \mathbf{u}' d\Omega$. We consider the case when an eigenmode, as defined by (10) and (11), is used as an initial condition for the computations. In this situation the kinetic energy can be expressed as $E(t) = \frac{\rho}{2} e^{2\lambda_r t} \int_{\Omega} \bar{\mathbf{u}} \cdot \bar{\mathbf{u}} d\Omega$. Here, the overbar indicates the complex conjugate while

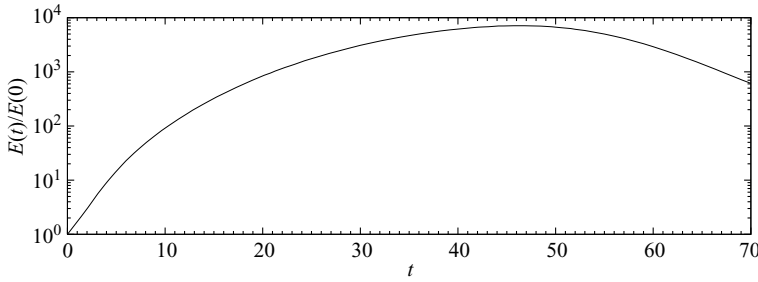


FIGURE 13. $H = 10$, $Re = 500$ flow past a half-cylinder: time history of the normalized disturbance energy ($E(t)/E(0)$) computed from the linearized disturbance equation. The initial disturbance field is the most unstable mode for $c_x = 0.8$ ($c_y = 0$) obtained from the global linear stability analysis.

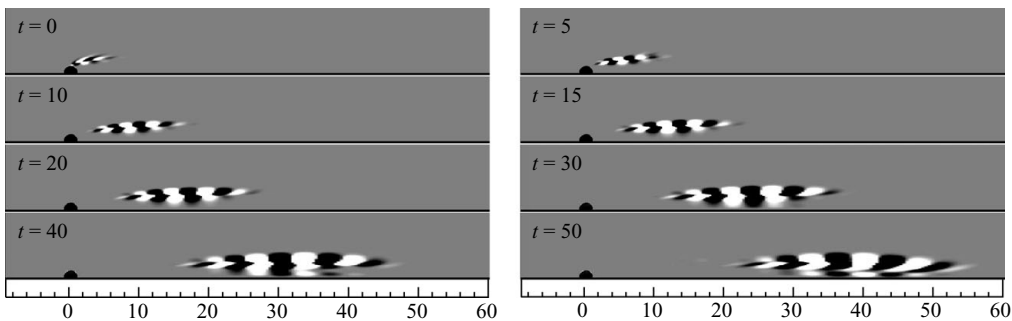


FIGURE 14. $H = 10$, $Re = 500$ flow past a half-cylinder: snap shots of the disturbance vorticity field at different time instants (see the caption of figure 13 for details).

λ_r is the growth rate of the mode. This leads to the following expression for an estimate of λ_r

$$\lambda_r = \frac{1}{2t} \ln \frac{E(t)}{E(0)}. \quad (17)$$

Figure 13 shows the time history of the kinetic energy of the disturbance for the $Re = 500$ flow with $H = 10$ when the computations are initiated with the most unstable mode moving with $c_x = 0.8$ and $c_y = 0.0$. Exponential growth of the energy is seen at the beginning of the computation followed by a plateau and then a fall-off as the disturbances are washed out of the domain. The time evolution of the vorticity field of the disturbance is shown in figure 14. The disturbances grow as they are convected downstream leading to an increase in $E(t)$ with time. Using the value of energy at $t = 5$ and the expression given by (17) the growth rate is found to be $\lambda_r \sim 0.268$. This value is in good agreement with that from the linear stability analysis that predicts $\lambda_r \sim 0.263$. The convective speed of the disturbance from this figure is also estimated to be close to 0.8 for t near 0. The good agreement in the results from the linear stability analysis and the direct time integration of the linearized disturbance equations adds to our confidence in the present analysis. At this point we note that, since the modes under consideration are convectively unstable, the energy estimate given by (17) is valid only in the frame travelling with the mode. However, for small t , the parts of the domain that differ between the laboratory and moving frames contain little energy.

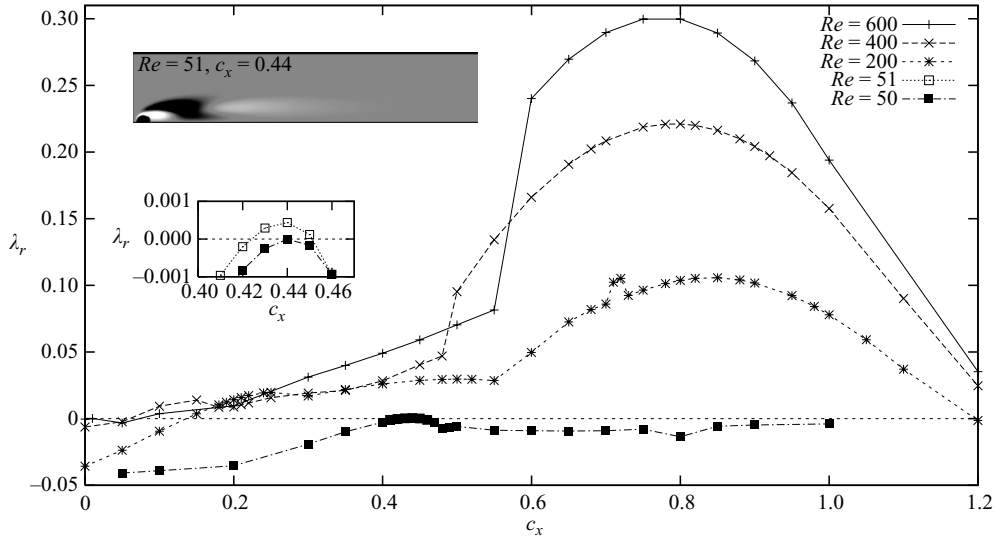


FIGURE 15. Linear stability analysis for the $H = 10$ flow past a half-cylinder: variation of the growth rate of the most unstable eigenmode with c_x for different Re . Only streamwise travelling modes are considered ($c_y = 0$). The vorticity field of the unstable eigenmode close to the onset of the instability ($Re = 51$, $c_x = 0.44$) is also shown.

From figure 13 it is seen that the energy ratio grows up to ~ 7000 in about 50 time units. Similar kinds of rapidly growing disturbances have been reported earlier in other situations. For example, Fasel & Postl (2006) showed that the steady-state separation bubble of the boundary layer over a flat plate is associated with large convective growth. This leads to growth of perturbations by several orders of magnitude. As a result extremely small environmental disturbances can grow and lead to instabilities which are not intrinsic to the flow. A similar situation can arise in numerical computations in flows that are marginally absolutely stable but highly unstable with respect to convective disturbances. Despite the flow being absolutely stable, this can lead to sustained instabilities because of very large growth of round off errors. Such high growth can also cause the nonlinear effects to become prominent leading to the possibility of subcritical bifurcation. This aspect, however, has not been investigated in the present work.

5.4.3. $H = 10$, critical Re for the onset of shear layer instability

We now seek the critical Re for which the shear layer instability appears for $H = 10$. Computations are carried out for various Re . At each Re the stability of the convective modes is evaluated for various values of c_x . The lowest value of Re at which the growth rate of any of the convective modes becomes unstable is Re_c . Figure 15 shows the variation of growth rate with c_x for different values of Re . Only streamwise moving disturbances are considered, i.e. $c_y = 0$. We can see that the flow becomes convectively unstable beyond $Re = 50$. In the same figure the vorticity field of the unstable eigenmode at the critical condition ($c_x = 0.44$, $Re = 51$) is also shown. This mode is found to be purely real. We note that the vortical structures in the mode are relatively large compared to what have been observed at large Re in experiments by earlier researchers. The shear layer vortices become smaller as Re increases.

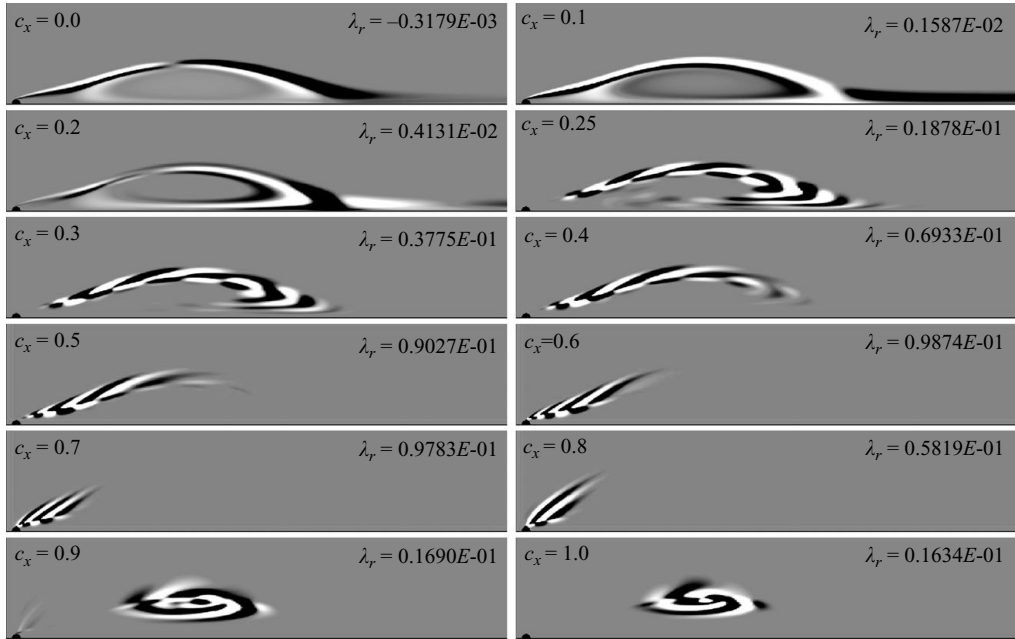


FIGURE 16. Linear stability analysis of the $H = 50$, $Re = 500$ flow past a half-cylinder: vorticity field of the real part of the most unstable mode for different values of c_x (growth rates are also shown). Only streamwise travelling modes are considered ($c_y = 0$).

5.4.4. Effect of blockage on Re_c for the onset of shear layer instability

In the previous section results were presented for $H = 10$. Such large blockage is expected to significantly alter the flow as compared to that in an unbounded flow situation. A question that comes to mind is the effect of blockage on the onset of shear layer instability. We, therefore, examine results for larger values of H .

Our results for the case of $H = 50$ shows that the growth rate, in general, increases with increase in Re . The variation of λ_r with c_x , for each Re , is interesting. For larger Re , λ_r first increases and then decreases as c_x increases. The critical Re for the onset of convective instability for $H = 50$ is $Re = 54$. This value is a little larger than the critical Re for $H = 10$. In general, for a given Re , the growth rate for $H = 50$ is smaller than that for $H = 10$. Hence, we conclude that as the sidewalls are brought closer the instability becomes stronger.

Figure 16 shows the real part of the most unstable modes obtained for different values of c_x at $Re = 500$ and $H = 50$. The corresponding growth rates of the modes are also shown. The modes can be classified in one of the three types. The first type of modes are the ones which have bubble-like structure in the wake. These can be seen for $c_x = 0.0, 0.1$ and 0.2 . The second type of modes have small-scale structures in the shear layer emanating from the cylinder. This type of modes are observed for $0.25 \leq c_x \leq 0.8$ and are very typical of the shear layer vortices that have been observed in experiments at larger Re . The third type of modes, for $c_x = 0.9$ and $c_x = 1.0$, resemble a tornado. These modes have very low growth rate. However, if excited sufficiently, they could lead to tornado type of motion. It is possible that for very high Re they may show large growth rate.

5.4.5. $H = 50$, $Re = 500$: direct time integration of the disturbance equations

The time evolution of the disturbance is computed via time integration of the nonlinear disturbance equations. The initial condition is the steady flow perturbed by

a very small randomized velocity field having amplitude of the order of 5.0×10^{-5} . Unlike the linearized disturbance equations, the nonlinear equations limit the growth of disturbance amplitude. It is observed that the disturbances, which resemble the shear layer modes predicted by the global linear stability analysis, develop with time. After an initial growth they start decaying. At $t \sim 1000$ the disturbance resembles the modes which are predicted by the stability analysis for low values of c_x (figure 16). These modes have long streaks of vorticity along the shear layer. The simulation testifies to the fact that the modes which have larger growth rate dominate the flow and those which have larger speeds leave the flow field earlier. The time evolution of the disturbance starting from the most unstable convective mode, i.e. the mode for $c_x = 0.6$, is also carried out via integration of the linearized disturbance equations. Large transient growth similar to that for $H = 10$ is observed.

5.4.6. Comparison of present results with those from local analysis

In the past, local analysis has been carried out for various cases of shear flows (Huerre & Monkewitz 1985; Hultgren & Aggarwal 1987; Castro 2005). While Huerre & Monkewitz investigated the hyperbolic tangent profile, Hultgren & Aggarwal and Castro investigated the Gaussian profile. In the later two cases the investigations were also carried out with the symmetry condition imposed at the centreline. Castro, in his investigation, also considered the flow bounded by slip walls placed at finite distance.

We compare our results from the global stability analysis of the non-parallel flow with those from earlier researchers. We consider two cases, $H = 10$ and $H = 50$. Recall, the critical Re for the onset of convective instability, from the global stability analysis, for the two values of H is 51 and 54, respectively. Using the computed profiles we estimate the local Reynolds number Re_l based on the maximum velocity defect ($= s(x) u(x, y = H)$) and the wake half-width. The parameter $s(x)$ is computed with the help of the expression

$$s(x) = \frac{u(x, y = H) - u(x, y = 0)}{u(x, y = H)}.$$

The wake half-width $b(x)$ is the vertical distance from the wake centreline where the velocity defect with respect to $u(x, y = H)$ is one-half the maximum defect at each location ($= u(x, H) - u(x, 0)$).

It is found from our computations that the Re_l shows substantial streamwise variation and achieves a maximum value of ~ 45 for $H = 10$. The maximum for $H = 50$ is slightly lower. For the same Re , based on the diameter of the cylinder, the maximum local Reynolds number is higher for smaller H . The larger Re_l for $H = 10$ is a consequence of the larger local increase in the streamwise speed for the higher blockage. The critical Re for convective instability predicted by Castro (2005) for $H = 10$ is 53.06. The maximum value of Re_l from the present analysis is lower (~ 45). This value is achieved in the near wake of the cylinder. It is found that, in the near wake, the velocity profiles for the base flow from the direct numerical simulations are quite different than the Gaussian profile utilized by Castro. Therefore, a difference in the results from the two methods is not surprising. In fact, it is quite interesting that the two approaches lead to comparable values of Re_c that are different by less than 20 %.

5.4.7. $H = 10$, $Re = 500$ and non-zero c_y

So far we have restricted ourselves to streamwise travelling disturbance waves, i.e. $c_y = 0.0$. In general, a disturbance can travel in any direction. Is it possible that the

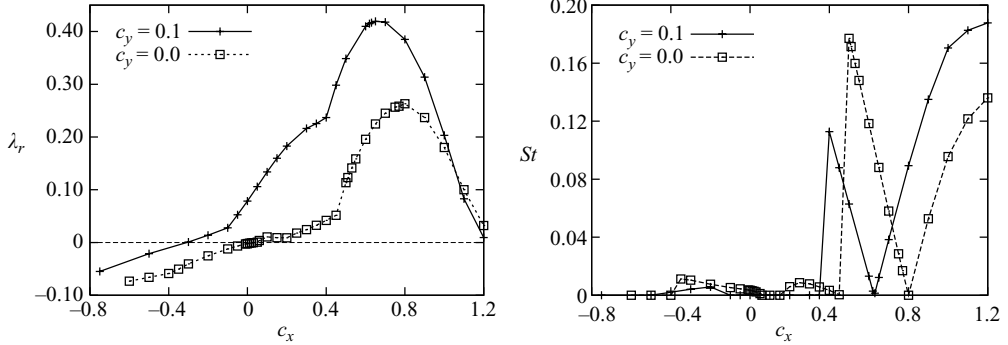


FIGURE 17. Linear stability analysis of the $H = 10$, $Re = 500$ flow past a half-cylinder: variation of the growth rate and St with c_x for two different values of c_y ($= 0.0$ and 0.1).

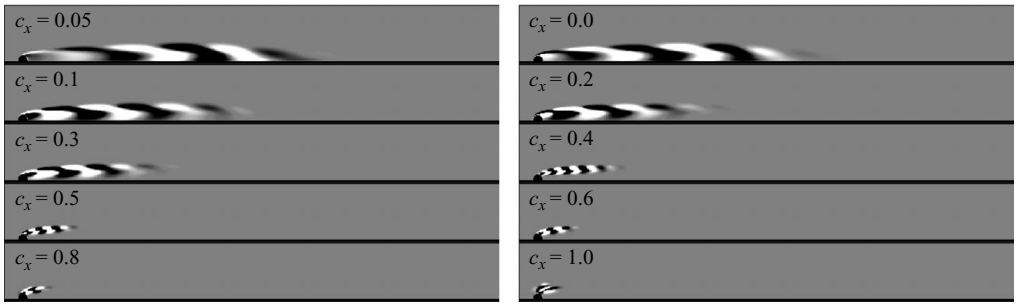


FIGURE 18. Linear stability analysis of the $H = 10$, $Re = 500$ flow past a half-cylinder: vorticity field of the real part of the most unstable mode for various values of c_x (and $c_y = 0.1$).

growth rate of a wave travelling in any other directions could be more? To investigate this we carry out linear stability analysis with non-zero value of c_y . We begin with $c_y = 0.1$. Figure 17 shows the results from the computations. The variation of growth rate and St with c_x are shown. For comparison, the results from $c_y = 0$ are also shown. It is seen from the figure that the results for $c_y = 0$ and $c_y = 0.1$ are very similar, qualitatively. However, the maximum value of the growth rate is higher for $c_y = 0.1$ and the maxima occurs at $c_x \sim 0.7$. For $c_y = 0.0$ the maximum growth rate occurs for $c_x \sim 0.8$. The real part of the most unstable modes for various values of c_x are shown in the figure 18. Comparing the modes for $c_y = 0$ and $c_y = 0.1$, shown in the figures 12 and 18, respectively, we observe significant differences for low values of c_x . For $c_y = 0.0$ the modes have larger scale vortical structures in the wake for low values of c_x . For larger c_x the mode shapes are very comparable.

It is also observed from figure 17 that the disturbances travelling in the crossflow direction ($c_x = 0$, $c_y = 0.1$) are convectively unstable. We, therefore, investigate the effect of c_y while c_x is kept zero, i.e. waves that travel purely in the crossflow direction. If indeed some such waves have growth rate that are larger than other waves, they can grow and be seen in experiments. This possibility exists and is, perhaps, more likely in a non-parallel flow. Figure 19 shows the growth rate and Strouhal number variation with the cross-stream speed c_y for $c_x = 0$, of the most unstable modes. The real part of the corresponding modes are shown in the figure 20. We observe that, in general, the growth rate of these modes are relatively smaller than the streamwise moving modes. Hence these modes will get dominated by others. The maximum growth rate

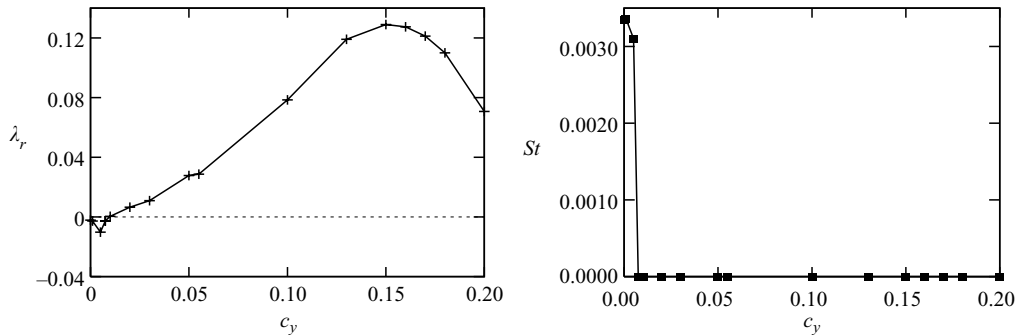


FIGURE 19. Linear stability analysis of the $H = 10$, $Re = 500$ flow past a half-cylinder: variation of the growth rate and St with c_y . Only crossflow moving disturbances are considered ($c_x = 0.0$).

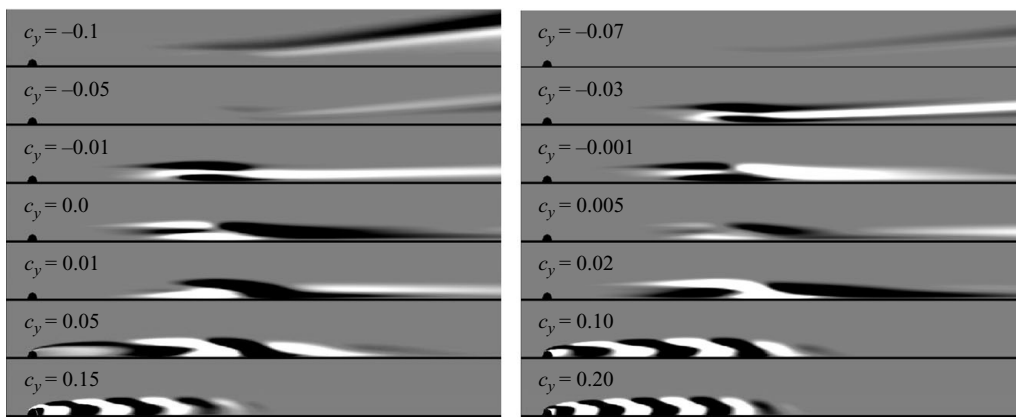


FIGURE 20. Linear stability analysis of the $H = 10$, $Re = 500$ flow past a half-cylinder: vorticity field of the real part of the most unstable mode for various values of c_y . Only crossflow moving disturbances are considered ($c_x = 0.0$).

occurs around $c_y = 0.15$ and the corresponding mode has small-scale structures in the wake which are very similar to those seen for the streamwise moving disturbances.

The global analysis in the present work, of perturbations in a moving frame, has significant parallels with the local analysis carried out by Healey (2006) and Juniper (2007). As opposed to the usual parallel flow analysis which considers the disturbance velocity in the streamwise direction only, Juniper carried out the analysis for perturbations which could move in the cross-stream direction as well. It was found that for unconfined flows the behaviour at $t = 0$ was a good representation for the behaviour at large times. However, in the case of confined flows a very interesting observation was made. The disturbance waves get reflected from the lateral walls and set up a standing wave that is not captured by the behaviour at $t = 0$.

6. Conclusions

Global absolute and convective stability analysis has been carried out for the cylinder wake with centreline symmetry. The base flow is the steady flow computed for one-half of the domain with free-slip conditions on the symmetry plane. Various locations of the lateral boundary are considered. The results are in very good

agreement with those reported earlier (Fornberg 1985; Fornberg 1991; Gajjar & Azzam 2004).

The linear stability analysis of the steady flow has been carried out via an eigenvalue formulation to get the most unstable modes and the corresponding frequencies. The growth rate shows a non-monotonic variation with Re . This behaviour is more pronounced for higher blockage. The non-monotonic variation is primarily caused by the decrease in the shear of the base flow as one moves downstream in the wake. The corresponding St shows a monotonic decrease with increase in Re . The critical Re for the onset of absolute instability has been found for various values of H . The variation of Re_c with H also shows a non-monotonic behaviour. The minimum Re_c is observed for $H = 15$. The non-monotonicity is caused by the dual role of the lateral boundary in both stabilizing and destabilizing the flow. Similar non-monotonic variation of Re_c with blockage has been reported earlier for the primary wake instability (Kumar & Mittal 2006a; Kumar & Mittal 2006b). Castro (2005) carried out full nonlinear computations for flow past a normal flat plate with free-slip conditions on the symmetry plane. Unlike the present results, he found that the Re_c for the onset of unsteadiness decreases with increase in H . This suggests that either the non-monotonicity is specific to the cylinder or the flow past a flat plate needs to be examined for lower blockage. More work is needed to resolve this issue. Generally, the most unstable mode for all H have bubble-like structure in the near wake followed by long streaks of vorticity in the far wake. We refer to these modes as bubble modes. It is shown that they are responsible for the low-frequency expansion and contraction of the recirculation bubble. Such low-frequency oscillations have been observed in flows earlier (see Alam & Sandham 2000; Manhart & Fredrich 2001; Castro 2005).

Castro (2005) proposed, from physical arguments, that the time period T of these oscillations varies as ReH^2 . However, from his direct numerical simulations he found that the slope of the T versus ReH^2 is closer to 2 than to 1. Our results from the linear stability analysis also show that the slope is larger than 1. In general, the slope increases with increase in H . In fact, T increases very rapidly with ReH^2 for larger values of H . The results suggest that the time period approaches infinity with H , i.e. the bubble mode instability might disappear for a truly unbounded flow. More work needs to be done to ascertain this. The St , at the onset of instability, from the present analysis shows a monotonic decrease with decrease in blockage. It is found that Re_c increases very rapidly as the lateral boundaries are moved away from the cylinder beyond $H = 15$. This also motivates us to speculate that, for low blockage, the flow might remain stable to the bubble mode up to fairly high Re .

Direct time integration of the full nonlinear flow equations has been carried out for the $Re = 750$ flow for $H = 10$. The time histories of C_L and C_D show oscillations on two different time scales. The large time scale or low-frequency oscillations correspond to the expansion/contraction of the wake bubble and release of large-scale vortices. The small time scale or high-frequency oscillations are due to the small-scale vortices which are a consequence of the instability of the separated shear layer from the cylinder. This has been ascertained via a global stability analysis for convective disturbances following the method presented by Mittal & Kumar (2007).

The critical Re for small-scale disturbances (shear layer instability) has been a contentious issue for a while. Various values of Re_c have been proposed in the past: = 1300 by Bloor (1964), beyond 350 by Gerrard (1978), beyond 1900 by Unal & Rockwell (1988), beyond 1200 for parallel shedding by Prasad & Williamson (1997) and beyond 740 by Rajagopalan & Antonia (2005). Global linear stability analysis has

been carried out for various speeds of the disturbance. The critical Re for the onset of shear layer instability, from the present analysis, is found to be 51 and 54 for $H = 10$ and $H = 50$, respectively. The $H = 50$ is a good approximation to the unbounded flow, at least at Re as low as 54. The scatter in the data from experiments regarding Re_c can be explained by the fact that the shear layer instabilities are convective in nature. Therefore, their appearance in experiments or computations is largely dependent on the background disturbance. Furthermore, at low Re they can be overshadowed by the more dominant wake modes.

In general, the convective modes can travel in any direction. It is found from our computations, for $H = 10$, that modes that travel with a velocity having a small component in the cross-stream direction in addition to streamwise speed have larger growth rates as compared to the modes travelling strictly in the streamwise direction. Analysis has also been carried out for modes that travel in the crossflow direction only. Some modes of this kind are also found to be convectively unstable. The present results from the linear stability analysis are also supported by those from direct time integration of linearized disturbance equations. The time evolution of the energy of the disturbance show intermediate increase up to very high values before decaying. Such large increase in energy has also been observed earlier for other flow problems (Fasel & Postl 2006). This suggests that very small sustained background disturbances can grow to significant strength and be observed in a flow and give the same effect as a global absolute instability. The linear stability analysis for the $Re = 500$ flow for low blockage ($H = 50$) leads to three kinds of modes depending on the speed of the disturbance. Based on the vortical structures in the modes they are classified as the bubble, shear layer and tornado modes.

The results from the global analysis are compared with earlier results from local analysis (Hultgren & Aggarwal 1987; Castro 2005). For the Re_c from the global analysis, the streamwise variation of the local Reynolds number (Re_l), based on the maximum speed difference and the wake half-width, is determined for the base flow. Re_l shows substantial streamwise variation and achieves a maximum value of ~ 45 for $H = 10$. The maximum for $H = 50$ is slightly lower. The local analysis predicts about 20 % lower value. This difference might also be because the local analysis by Castro (2005) and Hultgren & Aggarwal (1987) was carried out for a synthetic velocity profile based on a Gaussian distribution. In the near wake the velocity profile from the present analysis are different from the Gaussian profile. However, they are in very good agreement in the far wake. It should be noted that all the computations in the present work are restricted to two dimensions. Since the Re considered is rather high it is possible that the actual flow might exhibit modes that are three-dimensional in nature. This will be investigated in a future study.

Partial support for this work from the Department of Science & Technology, India is gratefully acknowledged.

REFERENCES

- ALAM, M. & SANDHAM, N. S. 2000 Direct numerical simulation of a ‘short’ laminar separation bubbles with turbulent reattachment. *J. Fluid Mech.* **410**, 1–28.
- BLACKBURN, H. M., MARQUES, F. & LOPEZ, J. M. 2005 Symmetry breaking of two-dimensional time-periodic wakes. *J. Fluid Mech.* **522**, 395–411.
- BLOOR, M. S. 1964 The transition to turbulence in the wake of a circular cylinder. *J. Fluid Mech.* **19**, 290–304.

- BROOKS, A. N. & HUGHES, T. J. R. 1982 Streamline upwind/Petrov–Galerkin formulations for convection dominated flows with particular emphasis on the incompressible Navier–Stokes equations. *Comput. Methods Appl. Mech. Engng* **32**, 199–259.
- CASTRO, I. P. 2002 Weakly stratified laminar flow past normal flat plates. *J. Fluid Mech.* **454**, 21–46.
- CASTRO, I. P. 2005 The stability of laminar symmetric separated wakes. *J. Fluid Mech.* **532**, 389–411.
- CHEN, J. H., PRITCHARD, W. G. & TAVENER, S. J. 1995 Bifurcation for flow past a cylinder between parallel planes. *J. Fluid Mech.* **284**, 23–41.
- CHERNYSHENKO, S. 1988 The asymptotic form of the stationary separated circumfluence of a body at high Reynolds number. *Appl. Math. Mech.* **52**, 746–753.
- DING, Y. & KAWAHARA, M. 1999 Three-dimensional linear stability analysis of incompressible viscous flows using the finite element method. *Intl J. Numer. Methods Fluids* **31**, 451–479.
- FASEL, H. F. & POSTL, D. 2006 Interaction of separation and transition in boundary layers: direct numerical simulations. In *Sixth IUTAM Symposium on Laminar-Turbulent Transition*, pp. 71–88, Springer.
- FORNBERG, B. 1985 Steady viscous flow past a circular cylinder up to Reynolds number 600. *J. Comput. Phys.* **98**, 297–320.
- FORNBERG, B. 1991 Steady incompressible flow past a row of circular cylinders. *J. Fluid Mech.* **225**, 655–671.
- GAJAR, J. S. B. & AZZAM, N. A. 2004 Numerical solution of the Navier–Stokes equations for the flow in a cylinder cascade. *J. Fluid Mech.* **520**, 51–82.
- GERRARD, J. H. 1978 The wakes of cylindrical bluff bodies at low Reynolds number. *Phil. Trans. R. Soc. Lond. A* **288**, 351–382.
- GRIFFITH, M. D., THOMPSON, M. C., LEWEKE, T., HOURIGAN, K. & ANDERSON, W. P. 2007 Wake behaviour and instability of flow through a partially blocked channel. *J. Fluid Mech.* **582**, 319–340.
- HEALEY, J. J. 2006 A new convective instability of the rotating-disk boundary layer with growth normal to the disk. *J. Fluid Mech.* **560**, 279–310.
- HUDY, L. M., NAGUIB, A. M. & HUMPHRIES, W. M. 2003 Wall-pressure-array measurements beneath a separating/reattaching flow region. *Phys. Fluids* **15**, 706–717.
- HUERRE, P. & MONKEWITZ, P. A. 1985 Absolute and convective instabilities in free shear layers. *J. Fluid Mech.* **159**, 151–168.
- HUERRE, P. & MONKEWITZ, P. A. 1990 Local and global instabilities in spatially developing flows. *Annu. Rev. Fluid Mech.* **22**, 473–537.
- HUGHES, T. J. R. & BROOKS, A. N. 1979 A multi-dimensional upwind scheme with no crosswind diffusion. In *Finite Element Methods for Convection Dominated Flows* (ed. T. J. R. Hughes), AMD-vol. 34, pp. 19–35. ASME.
- HUGHES, T. J. R., FRANCA, L. P. & BALESTRA, M. 1986 A new finite element formulation for computational fluid dynamics. V. Circumventing the Babuška–Brezzi condition: a stable Petrov–Galerkin formulation of the Stokes problem accommodating equal-order interpolations. *Comput. Methods Appl. Mech. Engng* **59**, 85–99.
- HULTGREN, L. S. & AGGARWAL, A. K. 1978 Absolute instability of the Gaussian wake profile. *Phys. Fluids* **30**, 3383–3387.
- JACKSON, C. P. 1987 A finite-element study of the onset of vortex shedding in flow past variously shaped bodies. *J. Fluid Mech.* **182**, 23–45.
- JUNIPER, M. P. 2007 The full impulse response of two-dimensional jet/wake flows and implications for confinement. *J. Fluid Mech.* **590**, 163–185.
- KOCH, K. 1985 Local instability characteristics and frequency determination of self-excited wake flows. *J. Sound Vib.* **99**, 53–83.
- KUMAR, B. & MITTAL, S. 2006a Effect of blockage on critical parameters for flow past a circular cylinder. *Intl J. Numer. Methods Fluids* **50**, 987–1001.
- KUMAR, B. & MITTAL, S. 2006b Prediction of the critical Reynolds number for flow past a circular cylinder. *Comput. Methods Appl. Mech. Engng* **195**, 6046–6058.
- MANHART, M. & FREDRICH, R. 2001 DNS of a turbulent boundary layer with separation. In *Proceedings of the Second Conf. on Turbulence and Shear Flow Phenomena*, KTH, Stockholm.
- MARSDEN, J. E. & McCracken, M. 1976 *The Hopf Bifurcation and Its Applications*. Springer.
- MITTAL, S. 2008 Instability of the separated shear layer in flow past a cylinder: forced excitation. *Intl J. Numer. Methods Fluids* **56**, 687–702.

- MITTAL, S., KOTTARAM, J. J. & KUMAR, B. 2008 Onset of shear layer instability in flow past a cylinder. *Phys. Fluids* **20**, 054102–1–10.
- MITTAL, S. & KUMAR, B. 2003 Flow past a rotating cylinder. *J. Fluid Mech.* **476**, 303–334.
- MITTAL, S. & KUMAR, B. 2007 A stabilized finite element method for global analysis of convective instabilities in nonparallel flows. *Phys. Fluids* **19**, 088105–1–4.
- MORZYNSKI, M., AFANASIEV, K. & THIELE, F. 1999 Solution of the eigenvalue problems resulting from global non-parallel flow stability analysis. *Comput. Methods Appl. Mech. Engng* **169**, 161–176.
- NORBERG, C. 1994 An experimental investigation of the flow around a circular cylinder: influence of aspect ratio. *J. Fluid Mech.* **258**, 287–316.
- NORBERG, C. 2001 Flow around a circular cylinder: aspects of fluctuating lift. *J. Fluids Struct.* **15**, 459–469.
- PRASAD, A. & WILLIAMSON, C. H. K. 1997 The instability of the shear layer separating from a bluff body. *J. Fluid Mech.* **333**, 375–402.
- RAJAGOPALAN, S. & ANTONIA, R. A. 2005 Flow around a circular cylinder-structure of the near wake shear layer. *Exp. Fluids* **38**, 393–402.
- SAAD, Y. & SCHULTZ, M. 1986 GMRES: a generalized minimal residual algorithm for solving nonsymmetric linear systems. *SIAM J. Sci. Stat. Comput.* **7**, 856–869.
- SADOVSKII, V. 1971 On local properties of vortex flows. *Uch. Zap. TsAGI* **4**, 117–120.
- SMITH, F. 1979 Laminar flow of an incompressible fluid past a bluff body: the separation, reattachment, eddy properties and drag. *J. Fluid Mech.* **92**, 171–205.
- STEWART, G. W. 1975 Methods of simultaneous iteration for calculating eigenvectors of matrices. In *Topics in Numerical Analysis II* (ed. J. H. H. Miller), pp. 169–185. Academic.
- TANG, S. & AUBRY, A. 1997 On the symmetry breaking instability leading to vortex shedding. *Phys. Fluids* **9**, 2550–2561.
- TEZDUYAR, T. E., MITTAL, S., RAY, S. E. & SHIH, R. 1992 Incompressible flow computations with stabilized bilinear and linear equal-order-interpolation velocity-pressure elements. *Comput. Methods Appl. Mech. Engng* **95**, 221–242.
- UNAL, M. F. & ROCKWELL, D. 1988 On the vortex formation from a cylinder. Part 1. The initial instability. *J. Fluid Mech.* **190**, 491–512.
- WILLIAMSON, C. H. K. 1989 Oblique and parallel modes of vortex shedding in the wake of a circular cylinder at low Reynolds numbers. *J. Fluid Mech.* **206**, 579–627.
- ZEBIB, A. 1987 Stability of viscous flow past a circular cylinder. *J. Engng Math.* **21**, 155–165.